Supporting Information

Nishida et al. 10.1073/pnas.1422194112

SI Text

Preparation of the [FeFe](dcbdt)$(CO)_6$-Functionalized UiO-66 MOF. [FeFe](dcbdt)$(CO)_6$ (Fig. S2*A*) was synthesized based on the previous report (1).

Solvothermal synthesis of UiO-66 MOF. A solid mixture of $ZrCl_4$ (16 mg, 0.07 mmol), 1,4-benzenedicarboxylic acid (11.6 mg, 0.07 mmol), and benzoic acid (427 mg, 3.5 mmol) was dissolved in DMF (4 mL). This solution was sealed in a 20-mL vial and heated to 120 °C. After 24 h of heating, the reaction mixture was allowed to cool to room temperature, after which the mixture was centrifuged for 15 min. The isolated solids were left to soak in MeOH for 3 d, and the mixture was centrifuged and exchanged with fresh MeOH (10 mL) every 24 h. After 3 d of soaking, the solids were isolated by centrifugation and dried under vacuum at room temperature.

Postsynthetic ligand exchange reaction to obtain UiO-66-[FeFe](dcbdt)$(CO)_6$ with 14% probe loading. The UiO-66 MOF prepared above was functionalized with postsynthetic ligand exchange reaction (2–4). [FeFe](dcbdt)$(CO)_6$ (50.8 mg, 0.1 mmol) was dissolved in deoxygenated Millipore water (2 mL). Deoxygnation was performed by bubbling Millipore water with N_2 (three times for 30 s each). UiO-66 (28 mg, ∼0.1 mmol equivalent of 1,4-benzenedicarboxylic acid) was added to the [FeFe](dcbdt)$(CO)_6$ solution, and the mixture was sonicated for 10 min to disperse UiO-66 particles into the solution. The solution was placed onto a shaker for 24 h at room temperature. After 24 h, the mixture was centrifuged, and the isolated solids were washed with copious amount of MeOH until the supernatant was colorless. The solids were left to soak in MeOH for 3 d, and the mixture was centrifuged and exchanged with fresh MeOH (10 mL) every 24 h. After 3 d of soaking, the solids were isolated by centrifugation and dried under vacuum at room temperature. As previously reported (1), this procedure gives UiO-66-[FeFe](dcbdt)$(CO)_6$ with 14% [FeFe] incorporation, which was evidenced by combustion analysis, ^{1}H NMR of digested MOF samples, and energy-dispersed X-ray spectroscopy. The sample was stored in a <20-ppm humidity dry box to avoid the adsorption of water. It has also been reported that the size of the MOF particles prepared in this procedure ranges from ∼200 nm to 500 nm. We assumed that, on average, the particle size is 300 nm and calculated the surface area to volume ratio. The volume of one particle is $\sim 1.4 \times 10^7$ nm^3, whereas the surface area is $\sim 2.8 \times 10^5$ nm^2. The size of the unit cell is known to be ∼1 nm (5). Thus, the unit cells at the surface are roughly 2% of the particle volume, and therefore, the surface will make a negligible contribution to the 2D IR signal.

Synthesis of UiO-66-[FeFe](dcbdt)$(CO)_6$ with lower probe loadings. To obtain UiO-66-[FeFe](dcbdt)$(CO)_6$ with lower probe loadings, the same ligand exchange reaction was used but with a lower molar ratio of [FeFe](dcbdt)$(CO)_6$ relative to UiO-66. Molar ratios [[FeFe](dcbdt)$(CO)_6$:UiO-66] of 0.035:1 and 0.25:1 were used to obtain lower loading samples. All of the samples were stored in a dry box. The actual loadings of the samples were determined by measuring the IR absorption spectra for each of the samples. The area ratios of the CO symmetric stretching mode at ∼2,077 cm^{-1} and the framework's background absorption around 1,800–1,900 cm^{-1} were compared with the ratio in the 14% sample (Fig. S1 *A–C*); the loadings were determined to be 0.2 ± 0.1% and 2.5 ± 1.1%, respectively.

Removal of physisorbed water and its effect on the vibrational probe. It is important to store all of the samples in the dry box to avoid the adsorption of atmospheric water. Cavka et al. (5) reported the removal of water in UiO-66 MOF by heating the sample up to 250 °C under vacuum, although the same procedure could not be followed because of the heat sensitivity of the functional group [FeFe](dcbdt)$(CO)_6$. Instead, we found that storage of the UiO-66 MOF samples in the dry box for >1 d removes the major fraction of physisorbed water as confirmed by the FTIR spectra (Fig. S1 *D* and *E*). The broad absorption centered around ∼3,400 cm^{-1} vanished after storage in the dry box, and the sharp peak at ∼3,672 cm^{-1} became more evident. The sharp peak was previously assigned to the μ_3-OH stretching mode in the Zr metal cluster (5). It is known that Zr clusters can be in either hydroxylated or dehydroxylated forms. The existence of the μ_3-OH stretching mode shows that the UiO-66 MOFs studied here are in the hydroxylated form. The sharp peak at 3,672 cm^{-1} is accompanied by the structured tail at 3,630–3,660 cm^{-1}. A similar structure has been observed in a previously reported functionalized UiO-66 MOF (6). This feature could indicate a small remnant of water in the pores, but considering that the amount is very minor compared with the fully hydrated sample in Fig. S1*D*, it is unlikely that this water alters the structural dynamics of the MOF. Importantly, the significant change in the CO stretching mode of the incorporated [FeFe](dcbdt)$(CO)_6$ was observed on the removal of the adsorbed water as well (Fig. S1 *D*, *Inset* and *E*, *Inset*). FTIR, 2D IR, and pump-probe measurements were applied only to the dried samples to exclude the possibility that the water dynamics in the pores are the source of the observed dynamical properties.

Immersion in DMF. When the dynamical properties of the MOFs in DMF were measured, the MOFs were immersed in DMF solvent during the experiment. Assuming that the density of DMF in the framework is the same as its density in bulk liquid, we estimated the number of DMF molecules to be five or six per one octahedral pore.

FTIR Spectroscopy. [FeFe](bdt)$(CO)_6$ (Fig. S2*B*) was synthesized according to a previous report (1). Fig. S2 *C–E* shows the FTIR spectra (0.5-cm^{-1} resolution) for the dry functionalized UiO-66 MOF with 2.5% loading (Fig. S2*C*), the functionalized 2.5% UiO-66 MOF immersed in DMF (Fig. S2*D*), and a 3.3 mM solution of [FeFe](bdt)$(CO)_6$ in DMF (Fig. S2*E*). The details are discussed together with the results from 2D IR spectroscopy in *Results and Discussion*.

Scattering Removal Scheme in 2D IR Spectroscopy. The scattering removal scheme used here is essentially identical to the one recently used by Baiz et al. (7) to eliminate the pump beams in a fully collinear geometry for 2D IR microscopy. The signals detected by the HgCdTe detector can be written as

$$\begin{aligned} &|E_{LO} + E_{sig} + s_1E_1 + s_2E_2|^2 \\ &= \left(|E|^2 \text{ terms}\right) + E^*_{LO}E_{sig} + s_1E^*_{LO}E_1 \\ &+ s_2E^*_{LO}E_2 + s^*_1s_2E^*_1E_2 + \text{c.c.}, \end{aligned} \qquad \textbf{[S1]}$$

where E_{LO} is the local oscillator E field, E_{sig} is the echo signal's E field, and s_1E_1 and s_2E_2 are the scattered E fields from the two pump pulses E_1 and E_2, respectively; s_1 and s_2 are complex scattering coefficients. All of the $|E|^2$ terms are phase-independent and thus, removed by phase cycling. $E^*_{LO}E_{sig}$ is the heterodyned signal of interest. $s_1E^*_{LO}E_1$ and $s_2E^*_{LO}E_2$ are the dominant terms of the scattering artifacts that can be removed by four-shots phase cycling of the pump pulses given by

$$[(0,0)-(0,\pi)]+[(\pi,\pi)-(\pi,0)], \quad \textbf{[S2]}$$

where (φ_1,φ_2) is the intensity on the detector obtained with the phases of pump pulses 1 and 2 set to φ_1 and φ_2, respectively (8).

When s_1 and s_2 are large, $s_1^* s_2 E_1^* E_2$ becomes dominant as well, and this term has exactly the same phase dependence as the echo signal on E_1 and E_2 ($E_{sig} \propto E_1^* E_2 E_3$). To avoid the scattering contamination from this term, the polarizations of the pump beams were set vertical, whereas the polarizations of the probe were set horizontal and resolved by a horizontal polarizer after the sample. The major fraction of the pump scattering was removed by the resolving polarizer. The signal to scattering artifact ratio was greatly improved by this polarization scheme.

Depending on the sample, particularly when the sample was thicker than >100 μm, the polarization scheme mentioned above was not sufficient to completely remove the scattering artifacts ($s_1^* s_2 E_1^* E_2$). The incomplete scattering removal is possibly because of the leakage of the pump pulses from the polarizer or the depolarization caused by the sample particles. Thus, for these thick samples, in addition to the <*XXYY*> polarization scheme, the probe was chopped with one-half of the repetition rate of the IR pulses, and the following eight-shot phase cycling was used to purely extract the $E_{LO}^* E_{sig}$ term (7):

$$\begin{aligned}&[\{(0,0,\mathrm{OFF})-(0,0,\mathrm{ON})\}-\{(0,\pi,\mathrm{OFF})-(0,\pi,\mathrm{ON})\}]\\&+[\{(\pi,\pi,\mathrm{OFF})-(\pi,\pi,\mathrm{ON})\}-\{(\pi,0,\mathrm{OFF})-(\pi,0,\mathrm{ON})\}],\end{aligned} \quad \textbf{[S3]}$$

where (φ_1,φ_2,chop) is the intensity on the detector with the phases of pump pulses 1 and 2 set to φ_1 and φ_2 and the chopper set to either OFF (unblock the probe) or ON (block the probe). When the probe (the LO) is blocked, all of the terms (except for the $s_1^* s_2 E_1^* E_2$ term) are removed. Thus, by subtracting this term from the intensity obtained with the unblocked probe, $E_{LO}^* E_{sig}$ + ($|E|^2$ terms) + $s_1 E_{LO}^* E_1$ + $s_2 E_{LO}^* E_2$ is left, from which $E_{LO}^* E_{sig}$ is extracted by the phase-cycling scheme already discussed. The 2D IR spectra obtained in these scattering removal schemes are shown in Fig. 2 *A* and *B* and are clearly free from the scattering artifact. Before all of the measurements, the 2D spectra were acquired at T_w = 250 ps (where the echo signal has vanished because of the vibrational relaxation) to assure that all of the scattering-related terms are completely removed to show no feature along the diagonal line.

Suppression of CLS Oscillation. As discussed in the text, the vibrational probe has four IR active vibrational modes that are coupled to each other. It turns out that these couplings cause the oscillation in the band shape (and thus, CLS) (Fig. 3*B*) because of the unbalanced rephasing and nonrephasing signal contribution to the signal, which for off-diagonal peaks was previously simulated and referred to as a quasi-absorptive 2D band (9) and experimentally observed (10). Our result clearly indicates that the same thing can happen for the diagonal peak. The early time behavior of the 2D IR spectrum (taken with the scattering removal scheme discussed above) on the excitation of all of the four modes is shown in Fig. S3*A*. It is evident that the band shape is not fully absorptive and that some dispersive parts are observed in the 2D spectrum. In contrast, the 2D IR spectra in Fig. S3*B* obtained by the selective pumping scheme discussed in the text are free from contamination by the dispersive part.

The double-sided Feynman diagrams contributing to this symmetric mode's 2D band on the diagonal are shown in Fig. S4. When only one vibrational mode is selectively pumped, there are pairs of rephasing and nonrephasing signals each for ground-state bleaching and stimulated emission (Fig. S4 *A*–*D*), which yield a fully absorptive band when they are added together. However, when another mode coupled to the mode of interest is pumped together, there is another nonrephasing signal (Fig. S4*E*) that is not paired with a rephasing signal. After the second interaction, while the signals (Fig. S4 *A*–*D*) are all in the population state, the signal (Fig. S4*E*) is on a coherent oscillation with the difference frequency of the two modes, which is leading to the band shape oscillation with respect to T_w. As evidence of this mechanism, the Fourier transform of the oscillating CLS in Fig. 3*B* yields the frequency components corresponding to the separations between the vibrational modes (Fig. S3*C*).

In case the selective pumping scheme is used, as a tradeoff, the pump pulse is broadened in time. The square root of the holed pump pulse (intensity) spectrum shown in Fig. 3*A* was Fourier-transformed to yield the temporal structure of the pump pulse, which is shown in Fig. S5*A*. As seen there, the *E* field in time domain is broadened by the ringing pattern, but most of the *E* fields are included within ~500 fs, which is enough time resolution to extract >5-ps dynamics as discussed in the text. Careful attention has to be paid regarding what is the minimum T_w that is trustable; at very early T_w, pump and probe pulses are temporarily overlapped to generate a nonresonant signal, which can distort the 2D band shape. In such a nonresonant signal, because two interactions are involved from the selective pump pulse, the autocorrelation of the pump *E* field is the quantity of interest that must be evaluated. As seen in Fig. S5*B*, at t = 2 ps, the autocorrelation decays by two orders of magnitude. Considering that the contribution from the nonresonant signal is, at most, 10% of the echo signal of interest (based on the pump-probe measurement at T_w = 0 ps), at T_w = 2 ps, the observed signal should be free from the nonresonant signal. Thus, all of the dynamical time constant extracted from the measurements are based on the measurements taken after T_w = 2 ps.

Orientational Correlation Function With and Without Solvent. As discussed in the text, the evaluation of the loading-dependent anisotropy decay was critically important for the quantitative estimation of the excitation transfer process. The data are shown in the text for the dry samples. The same experiment was done on the samples immersed in DMF and is shown in Fig. S6 together with the dry sample. The decays in 14% and 2.5% samples with and without solvents are well-reproduced by the excitation transfer-induced anisotropy decay in the form of $Ae^{-(t/\tau_{\mathrm{ET}})^{1/2}}$. Because τ_{ET} is inversely proportional to the square of the probe loading, at 0.2%, we estimate the τ_{ET} to be longer than ~50 ns with no solvent and ~90 ns in DMF, which is well beyond the timescale of the experiment. Thus, regardless of the presence of the solvents, at 0.2% sample, the contribution from the excitation transfer process is negligible. The solid lines in Fig. S6 for 0.2% samples are the fits in the form of $(r(0)-r(\infty))e^{-t/\tau_w}+r(\infty)$ following the wobbling-in-a-cone theory (11), and the fitting parameters are given in Table 1. It seems that the excitation transfer rate is even slower in DMF than in the dry samples. It is known that the Förster radius for the vibrational excitation transfer is dependent on not only the vibrational relaxation lifetime (T_1), the refractive index of the media, and the magnitude of the transition dipole moment, but also the complex interplays between homogeneous/inhomogeneous line widths and the spectral diffusion rate. All of these factors are affected on the immersion of the sample in DMF to lead to the different excitation transfer rate from the dry sample.

Isotropic Population Decay. The polarization-selective pump-probe experiment provides not only the anisotropy decay, but also the isotropic population decay calculated by $P(t)=S_{\parallel}(t)+2S_{\perp}(t)$. The obtained population decays with and without DMF are shown in Fig. S7 for the 0.2% sample. Each decay was fitted in the form of

$$P(t) \propto e^{-t/\tau_1} + re^{-t/\tau_2}, \quad \text{[S4]}$$

where τ_1 is the decaying time constant for the quick equilibration process between the four vibrational modes (note that only one mode is selectively pumped in the experiment), and τ_2 is the decaying time constant for the slow energy dissipation process. r is the amplitude ratio of these two contributions. The fitting curves are shown as the solid lines in Fig. S7, and the fitting parameters are given in Table S1. As is clear, the population decay is accelerated on immersion in DMF, because DMF provides the additional phonon modes to which the excited vibrational energy can be dissipated. These data indicate that DMF molecules are in close contact with the probe molecules, and thus, they are absorbed into the pores.

1. Pullen S, Fei H, Orthaber A, Cohen SM, Ott S (2013) Enhanced photochemical hydrogen production by a molecular diiron catalyst incorporated into a metal-organic framework. *J Am Chem Soc* 135(45):16997–17003.
2. Kim M, Cahill JF, Fei H, Prather KA, Cohen SM (2012) Postsynthetic ligand and cation exchange in robust metal-organic frameworks. *J Am Chem Soc* 134(43):18082–18088.
3. Fei H, Cahill JF, Prather KA, Cohen SM (2013) Tandem postsynthetic metal ion and ligand exchange in zeolitic imidazolate frameworks. *Inorg Chem* 52(7):4011–4016.
4. Karagiaridi O, Bury W, Mondloch JE, Hupp JT, Farha OK (2014) Solvent-assisted linker exchange: An alternative to the de novo synthesis of unattainable metal-organic frameworks. *Angew Chem Int Ed* 53(18):4530–4540.
5. Cavka JH, et al. (2008) A new zirconium inorganic building brick forming metal organic frameworks with exceptional stability. *J Am Chem Soc* 130(42):13850–13851.
6. Kandiah M, et al. (2010) Post-synthetic modification of the metal–organic framework compound UiO-66. *J Mater Chem* 20(44):9848–9851.
7. Baiz CR, Schach D, Tokmakoff A (2014) Ultrafast 2D IR microscopy. *Opt Express* 22(15):18724–18735.
8. Shim S-H, Zanni MT (2009) How to turn your pump-probe instrument into a multidimensional spectrometer: 2D IR and Vis spectroscopies via pulse shaping. *Phys Chem Chem Phys* 11(5):748–761.
9. Hamm P, Zanni MT (2011) *Concepts and Methods of 2D Infrared Spectroscopy* (Cambridge Univ Press, New York).
10. Wong DB, Giammanco CH, Fenn EE, Fayer MD (2013) Dynamics of isolated water molecules in a sea of ions in a room temperature ionic liquid. *J Phys Chem B* 117(2):623–635.
11. Tan HS, Piletic IR, Fayer MD (2005) Orientational dynamics of water confined on a nanometer length scale in reverse micelles. *J Chem Phys* 122(17):174501.

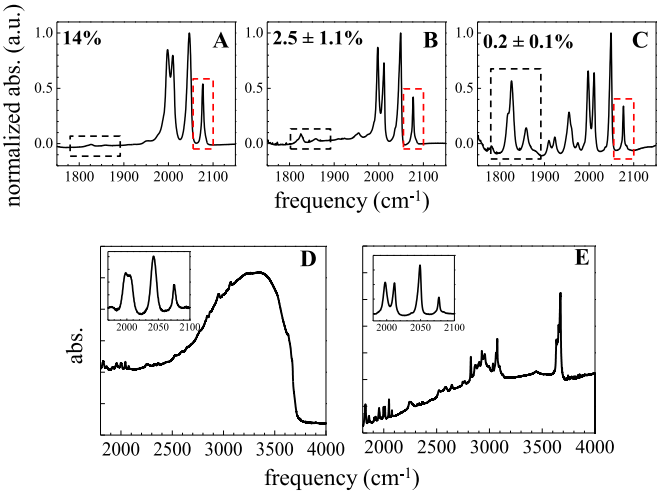

Fig. S1. (*A*–*C*) FTIR spectra for the functionalized MOF synthesized with [FeFe](dcbdt)$(CO)_6$: UiO-66 = (*A*) 1:1, (*B*) 0.25:1, and (*C*) 0.035:1. The probe loading in *A* is determined to be 14% by NMR and energy-dispersed X-ray spectroscopy. For the other samples, the loading was determined by calculating the area ratio of the CO symmetric stretching mode at ~2,077 cm^{-1} (red dotted squares) and the MOF's framework absorption band observed at 1,800–1,900 cm^{-1} (black dotted squares). (*D* and *E*) The 0.2% probe loading sample (*D*) before and (*E*) after storage in a dry box. (*Insets*) CO stretching regions. It is clear that the broad band centered around ~3,400 cm^{-1} from adsorbed water is removed in *E*.

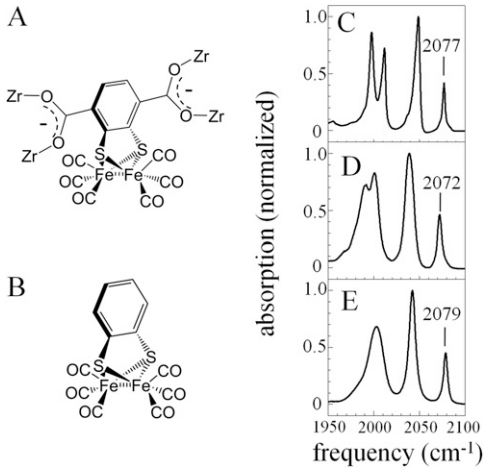

Fig. S2. (*A*) Molecular structure of the organic linker with the vibrational probe [FeFe](dcbdt)$(CO)_6$ incorporated into UiO-66. (*B*) Molecular structure of [FeFe](bdt)$(CO)_6$, the vibrational probe analog. (*C–E*) Linear IR absorption spectra for four CO stretching modes of (*C*) the functionalized UiO-66 MOF without solvent (dry), (*D*) the functionalized UiO-66 MOF immersed in DMF, and (*E*) the vibrational probe analog dissolved in bulk DMF.

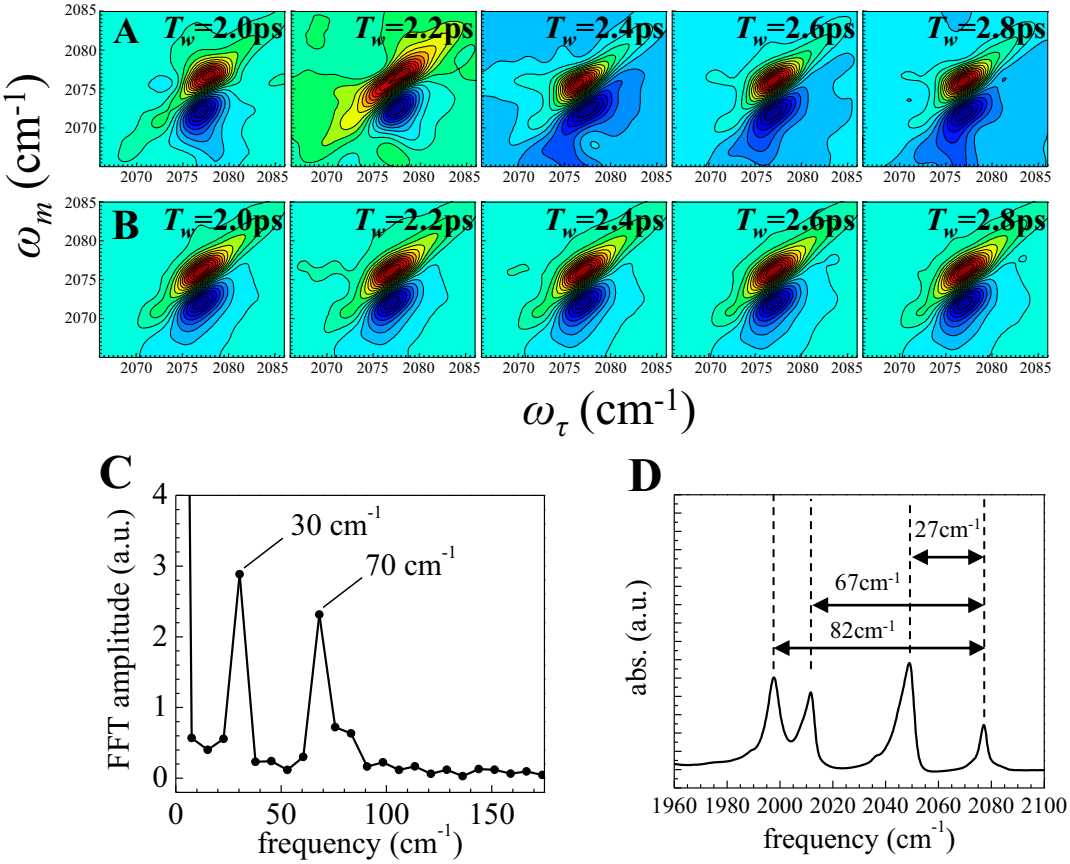

Fig. S3. (*A*) 2D IR spectra of the symmetric stretching mode for the 2.5% probe loading sample pumped with a full Gaussian spectrum pump pulse. (*B*) The same 2D band pumped with the spectrally holed pulse shown in Fig. 3*A*. (*C*) Fast Fourier transform (FFT) of the CLS measured with a full Gaussian spectrum pump pulse (black line in Fig. 3*B*). (*D*) The absorption spectrum of the 2.5% probe loading sample. The splitting between the bands corresponds well to the peaks in the Fourier transform of the CLS.

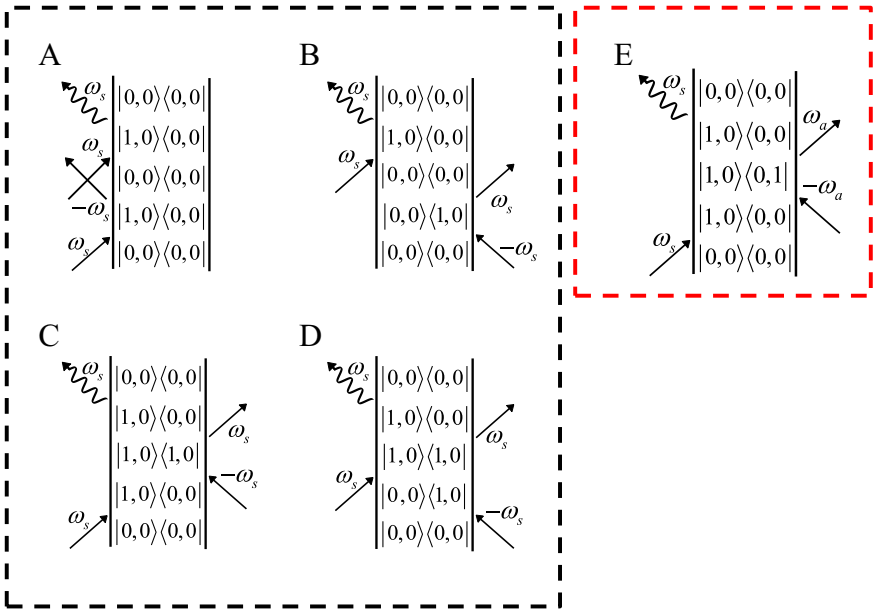

Fig. S4. Double-sided Feynman diagrams for the third-order response functions yielding the 2D signal at $(\omega_\tau,\omega_m)=(\omega_s,\omega_s)$. The ket $|s,a\rangle$ corresponds to the vibrational state with the symmetric stretching mode of interest *s* and one of three antisymmetric modes *a*. (*A* and *B*) Nonrephasing and rephasing signals for the ground-state bleaching, respectively. (*C* and *D*) Nonrephasing and rephasing signals for the stimulated emission, respectively. (*E*) The nonrephasing signal inducing the oscillation in the 2D band. The contribution from *E* is present only when another coupled mode is covered by both the pump and the probe pulses' spectra.

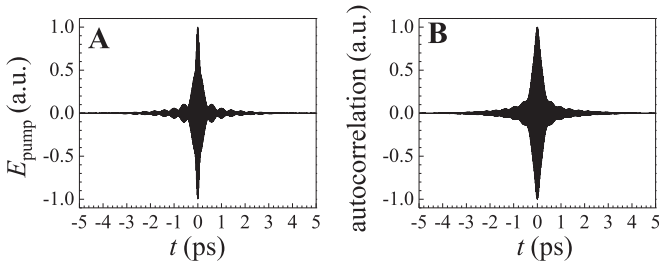

Fig. S5. (*A*) The spectrally holed pump pulse's *E* field in the time domain calculated as a Fourier transform of the square root of the frequency domain intensity spectrum given in Fig. 3*A* (red curve). (*B*) The autocorrelation of the *E* field given in *A*.

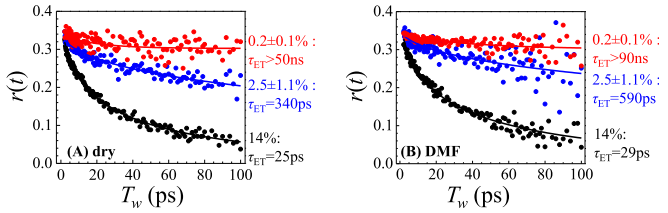

Fig. S6. The orientational correlation functions extracted from the anisotropy decays measured by polarization-selective pump-probe spectroscopy for (*A*) the dry samples with no solvent at $\omega_m=2{,}077$ cm^{-1} and (*B*) the samples immersed in DMF at $\omega_m=2{,}072$ cm^{-1}. The 0.2% samples were fitted well by the wobbling-in-a-cone model, whereas the higher loading samples were reproduced well with the excitation transfer model. Dots indicate data, and solid lines indicate fitting curves.

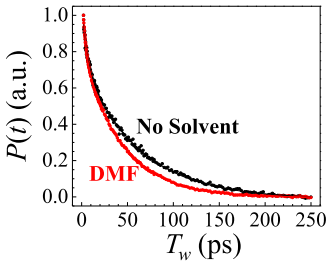

Fig. S7. The isotropic population decays measured by polarization-selective pump-probe spectroscopy for the dry 0.2% loading sample with no solvent at $\omega_m = 2{,}077\ cm^{-1}$ (black line) and the 0.2% loading sample immersed in DMF at $\omega_m = 2{,}072\ cm^{-1}$ (red line). Each decay was normalized at T_w = 2.1 ps. Dots indicate measured data points, and solid lines indicate the biexponential fitting curve.

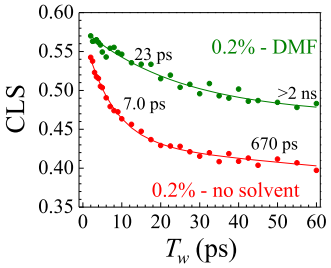

Fig. S8. The comparison of the CLS decays for the 0.2% loading MOF with and without DMF solvent (expanded view of Fig. 5). It is clear that the immersion of the MOF in DMF significantly slows down the CLS decay rate.

Table S1. The fitting parameters for the population decays in Fig. S7

Solvent	Probe loading (%)	τ_1 (ps)	τ_2 (ps)	r
No solvent	0.2	5.2	60.8	2.32
DMF	0.2	3.8	43.1	2.26

The curves were fitted in the form of expression **S4**.